

# Optimising Urban Measurement Networks for CO<sub>2</sub> Flux Estimation: A High-Resolution Observing System Simulation Experiment using GRAMM/GRAL

Sanam N. Vardag<sup>1,2,\*</sup> and Robert Maiwald<sup>1,\*</sup>

<sup>1</sup>Institut für Umweltphysik, Universität Heidelberg, Im Neuenheimer Feld 229, 69120 Heidelberg

<sup>2</sup>Heidelberg Center for the Environment, Universität Heidelberg, Im Neuenheimer Feld 229, 69120 Heidelberg

\*These authors contributed equally to this work.

**Correspondence:** Sanam N. Vardag (sanam.vardag@uni-heidelberg.de)

**Abstract.** To design a monitoring network for estimating CO<sub>2</sub> fluxes in an urban area, a high-resolution Observing System Simulation Experiment (OSSE) is performed using the transport model Graz Mesoscale Model (GRAMMv19.1) coupled to the Graz Lagrangian Model (GRALv19.1). First, a high-resolution anthropogenic emission inventory, which is considered as the truth serves as input to the model to simulate CO<sub>2</sub> concentration in the urban atmosphere on 10 m horizontal resolution in a 12.3 km x 12.3 km domain centered in Heidelberg, Germany. By sampling the CO<sub>2</sub> concentration at selected stations and feeding the measurements into a Bayesian inverse framework, CO<sub>2</sub> fluxes on neighbourhood scale are estimated. Different configurations of possible measurement networks are tested to assess the precision of posterior CO<sub>2</sub> fluxes. We determine the trade-off of between quality and quantity of sensors by comparing the information content for different set-ups. Decisions on investing in a larger number or more precise sensors can be based on this result. We further analyse optimal sensor locations for flux estimation using a Monte Carlo approach. We examine the benefit of additionally measuring carbon monoxide. We find that including CO as tracer in the inversion allows the disaggregation of different emission sectors. Finally, we quantify the benefit of introducing a temporal correlation into the prior emissions. The results of this study give implications for an optimal measurement network design for a city like Heidelberg. The study showcases the general usefulness of the developed inverse framework using GRAMM/GRAL for planning and evaluating measurement networks in an urban area.

*Copyright statement.* TEXT

## 1 Introduction

A large share of greenhouse gases (about 70 % of anthropogenic CO<sub>2</sub> emissions) is emitted in urban areas offering a huge potential to reduce greenhouse gas emissions (World Bank, 2010). To realise the full mitigation potential and to verify any emission reduction, solid knowledge of local greenhouse gas emissions is required. In addition to inventory-based (“bottom-up”) emission estimates, measurements of greenhouse gases can be used in an inverse framework to quantify emissions (“top-down”).

In a top-down approach, an atmospheric transport model is used to transport a best estimate of surface fluxes forward to obtain a simulated concentration field. The simulated concentrations are then compared to the measured concentration at the location and time of measurements. By varying the surface fluxes within their given uncertainties, the difference between measured and simulated concentrations is minimized to agree within the model-data uncertainties. In a Bayesian inverse framework, the result is the so-called posterior emission estimate. In the last years, many city CO<sub>2</sub> monitoring networks have formed at the local level. Monitoring systems in urban areas can be found in the San Francisco Bay Area (Turner et al., 2016; Delaria et al., 2021), Indianapolis (Turnbull et al., 2019; Oda et al., 2017; Lauvaux et al., 2016; Turnbull et al., 2015; Richardson et al., 2017; Deng et al., 2017; Davis et al., 2017; Balashov et al., 2020; Miles et al., 2021), Salt Lake City (Mallia et al., 2020; Kunik et al., 2019), Davos (Lauvaux et al., 2013), and Paris (Lian et al., 2022; Wu et al., 2016; Bréon et al., 2015). In future, it is expected that more networks will be installed supporting local mitigation endeavors (Jungmann et al., 2022). In order to optimise the investment in a measurement network and maximise the knowledge gained from these measurements, several parameters need to be considered preferably in the design-phase. These parameters include the number and location of nodes, the uncertainty of the measurements, and the co-measured species. They need to be optimised under consideration of a limited financial budget.

Observing System Simulation Experiments (OSSEs) offer a valuable tool for assessing different monitoring networks. OSSEs provide a controlled and consistent framework for assessing the performance of inversion methods used. In an OSSE emissions as well as atmospheric transport are known. The concentration is obtained by simulating the atmospheric transport of the emissions into the atmosphere. The concentration at selected sites can then be used in an inversion framework to estimate emissions. It is possible to e.g. add measurement uncertainty or model transport uncertainty to the concentration, or to change the prior emissions and evaluate the effect on the emission estimate by comparing to the known true emissions. Therefore, an OSSE enables isolating and analyzing various factors that contribute to uncertainties and errors in emission estimates. Therefore, an OSSE enables the analysis of different measurement network designs, facilitating the identification of optimal network configurations and providing insights into the inversion set-up characteristics. For instance, Turner et al. (2016) conduct an experiment using the actual sensor locations of the BEACON measurement network in the San Francisco Bay Area to assess the trade-off between low-cost sensors in higher quantities and fewer, but more expensive sensors with higher accuracy, by comparing the error in flux estimates for various set-ups. Their findings reveal two types of measurement network configurations: noise-limited configurations, where the inversion improves more substantially with higher sensor quality, and site-limited configurations, where the improvement is greater with an increased number of sensors. While Turner et al. (2016) select the sensor locations randomly from a fixed set of sensor locations, another study by Mano et al. (2022) develops an algorithm to determine optimal sensor locations for a measurement network. This algorithm utilises the entropy of expected trace gas concentration to identify ideal measurement positions. In a different study, Thompson and Pisso (2023) apply a Monte Carlo approach to optimise sensor locations. They are able to pinpoint the optimal sensor placement for CH<sub>4</sub> flux estimation from a set of possible sites in Europe. Thus, performing measurements at the selected sites improves the posterior emission estimates.

Furthermore, the CO<sub>2</sub> estimate may benefit from measuring co-emitted trace gases. For example, carbon monoxide (CO) is emitted together with CO<sub>2</sub> during fossil fuel combustion. The CO/CO<sub>2</sub> ratio varies with emission sectors and regions, which makes it potentially useful as a proxy for CO<sub>2</sub> emissions from fossil fuel combustion in general, and more specifically as a tracer

for traffic emissions (Vogel et al., 2010). Nathan et al. (2018) quantitatively analyse the advantages of CO as a trace gas in the inversion set-up using the INFLUX measurement network in Indianapolis. By incorporating CO measurements in the inversion, Nathan et al. (2018) successfully distinguish spatially overlapping sources into two sectors. Furthermore, the uncertainty of prior fluxes significantly affects the inversion process. Kunik et al. (2019) conduct an OSSE using a measurement network in Salt Lake City to examine the influence of the prior flux uncertainty. They demonstrate that incorporating realistic correlations in the prior between fluxes in the temporal and spatial dimensions can substantially improve the inversion results. Wu et al. (2018) obtain similar results regarding spatial correlation in the city of Indianapolis. These examples highlight the possibilities of OSSEs in analyzing urban network monitoring taking into consideration various aspects and site-specific characteristics. The resolution of urban OSSEs usually is 1 km or coarser and limited by the large computation time of the transport model, as well as by the inversion on a high resolution.

In our study, we employ the Reynolds-Averaged Navier Stokes model Graz Mesoscale Model (GRAMM) coupled to the Graz Lagrangian Model (GRAL) as a forward model (GRAMM/GRAL). Both models assume hourly steady-state conditions. Using the steady-state wind fields, GRAL simulates an hourly 10 m x 10 m concentration field at five heights per emission group within a 12.3 km x 12.3 km domain, accounting for the flow around buildings. This high resolution exceeds the typical 1 km resolution of previous OSSEs, enabling the use of any 10 m x 10 m grid cell as simulated concentration data for inversion, thus keeping the aggregation errors small. The high resolution is possible due to the comparatively cheap forward model when using the catalogue approach (see Sect. 2), as well as due to the hourly steady-state assumption of the model such that the Jacobian, i.e. the linearization of the forward model representing the sensitivity of the observation to the emissions, can be easily determined (see Sect. 2.2). This property allows for network optimization considering many different parameters and locations, including those affected by street channeling and surrounding buildings. Specifically, this study focuses on analysing sensor quantity versus quality, sensor location optimisation, the use of CO as an additional tracer, and the temporal correlation of the prior for the first time on high-resolution of 10 m x 10 m within a 150 km<sup>2</sup> domain centered on the Theodor-Heuss bridge in Heidelberg. With these first experiments, we also seek to showcase the general ability of the framework in general.

## 2 Methodology

### 2.1 The atmospheric transport model GRAMM/GRAL

Emissions and concentrations are linked via the atmospheric transport. Modelling the atmospheric transport is challenging due to turbulence. Especially for heterogenic urban environments, models need to account for different land use types and their associated properties, flow around buildings, and topography, which influence the atmospheric transport. For this task, there are two types of models, which are commonly used and which attempt to solve the Navier Stokes equation: Large Eddy Simulations (LES) and Reynolds-averaged Navier-Stokes simulations (RANS). While LES models explicitly solve large turbulent structures and parametrise small turbulent structures, RANS models use temporal averaging to reduce the complexity of the problem and generate steady-state flow fields. Therefore, RANS models are computationally cheaper compared to LES

90 models (Blocken, 2018). The model GRAMM/GRAL is a RANS model. Description of the model can be found in Berchet et al. (2017a, b), as well as in Öttl (2020).

GRAMM is a prognostic mesoscale model (Oetl, 2021) that computes hourly steady-state wind fields from synoptic forcing given parameters associated to land use cover such as surface roughness or thermal conductivity, and for a given topography of the domain. The synoptic forcing is determined by wind direction, wind speed, and a stability class to parameterise the  
95 turbulence. In this study, we chose a domain size of 20 km x 20 km centered on the Theodo-Heuss bridge in Heidelberg, Germany with a resolution of 100 m x 100 m. GRAL uses the GRAMM wind fields as mesoscale input and refines the wind fields to a higher resolution taking into account the flow around buildings. The GRAL domain size is 12.3 km x 12.3 km with a resolution of 10 m x 10 m. The vertical resolution of the wind field is 2 m with a total of 200 cells. The domain borders for GRAMM and GRAL are shown in Fig. 1. Hourly concentration fields are obtained in GRAL by transporting emissions  
100 in the GRAL domain forward. The emission types can be point, line, and area sources which can be grouped into up to 99 emission groups. An emission group is a set of emissions, which is stored and optimised together. For each emission group a concentration field can be obtained.

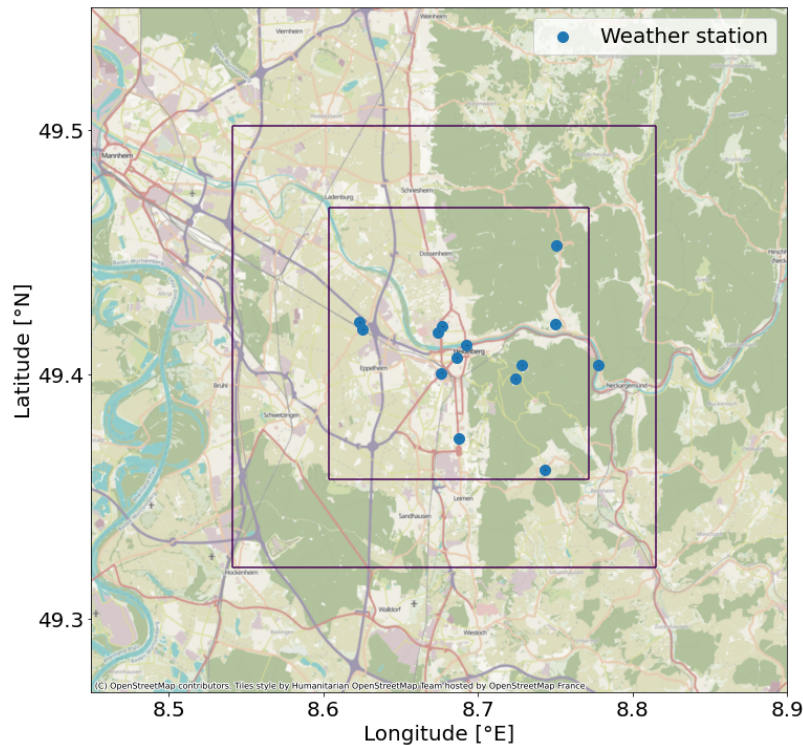


**Figure 1.** The outer box shows the GRAMM domain, which has an extent of 20 km x 20 km with a resolution of 100 m x 100 m. The inner box shows the GRAL domain with a size of 12.3 km x 12.3 km and a resolution of 10 m x 10 m. The blue dots denote the meteorological measurement stations for the matching algorithm. The administrative district borders lie within the GRAL domain and can be seen in Fig. C1.

In this study, the computational costs are further reduced by utilizing a catalogue approach. The catalogue approach exploits the fact that for longer periods similar weather situations reoccur. Utilizing the repetition of similar weather conditions, a catalogue of wind fields is computed covering all typical prevailing wind situations for the area. For Heidelberg, we use 1008 synoptic forcings, which are stored and are hourly matched with wind measurements to provide wind fields for the considered period. In particular, during the matching measured and pre-calculated simulated wind speeds and directions are compared hourly to find the pre-calculated wind situation that minimised the difference to measurements for that hour. Details can be found in Berchet et al. (2017a, b).

As the lifetime of CO<sub>2</sub> is much larger than the period of interest, the concentration enhancement of CO<sub>2</sub> in the atmosphere is proportional to the magnitude of the emissions. Using this linearity, a pre-computed concentration field can be scaled linearly to account for a change in the emissions. Emissions from an emission group can be scaled accounting for e.g. different temporal profiles due to a diurnal cycle of emissions. Note that emission groups do not have to be homogeneous, but may have a sub-structure. However, scaling the emission group then means scaling all emissions in their sub-structure. The total concentration enhancement field for a given time step is obtained as a sum of the concentration fields for each emission group. The choice of the emission groups should reflect the relative variability of the emissions sources such that grouped emissions should have a high correlation. The division into emission groups is described in Sect. 2.4.

## 2.2 The inverse framework

In this study, the inverse problem is estimating emissions  $x$  (state vector of length  $m$ ) from the forward modelled concentration measurements  $y$  (measurement vector of length  $n$ ). The relation between the measurements and the state vectors, i.e. emission groups per time step is given by the transport model GRAL.

$$y = \mathbf{K}x + \epsilon_y \quad (1)$$

with  $\epsilon_y$  as an vector of length  $n$  with Gaussian noise characterising the statistical uncertainty of the measurements. As CO<sub>2</sub> is inert on the timescales on which atmospheric transport in the city takes place, the concentration is proportional to the magnitude of the emissions, which means that the model is linear. The Jacobian matrix  $\mathbf{K}$  ( $m \times n$ ) fully describes the linear forward model and scales the concentration fields for each emission group. Each matrix  $\mathbf{K}$  for a given meteorological situation is constructed by simulating a concentration field for each emission group  $x_i$  with  $i \in (1, m)$ . The matrix entries  $K_{i,j}$  are the sensitivities of concentration of a specific measurement  $y_j$  with  $j \in (1, n)$  to changes in the emissions of the emission groups:

$$K_{i,j} = \frac{\partial y_j}{\partial x_i} \quad (2)$$

Depending on the emission scenario, a different linear combination of the emission groups forms the total concentration field of a given hour. As the problem is typically underconstrained and thus, no unique solution exists, regularization is required to obtain a stable and realistic solution. Therefore, we use a Bayesian inversion approach and constrain the solution  $x$  by introducing prior emissions  $x_a$  (vector of length  $m$ ) and prior error covariance  $\mathbf{S}_a$  ( $m \times m$  matrix) following Rodgers (2000):

$$\hat{x} = x_a + (\mathbf{K}^T \mathbf{S}_y^{-1} \mathbf{K} + \mathbf{S}_a^{-1})^{-1} \mathbf{K}^T \mathbf{S}_y^{-1} (y - \mathbf{K}x_a) \quad (3)$$

135 The uncertainties in  $y$  and  $\mathbf{K}$  are assumed to be Gaussian, unbiased, and independent of each other.  $\mathbf{S}_y$  ( $m \times m$  matrix) denotes the measurement covariance matrix, which we adjust within the OSSE (see Sect. 3.1). It contains instrument, model and representation errors. We assume that the matrix  $\mathbf{S}_y$  is diagonal, i.e. has no covariances, implying that the model and measurement errors are not correlated in time and space.

The posterior covariance  $\mathbf{S}_{\hat{x}}$  ( $n \times n$  matrix) is then given as:

$$140 \quad \mathbf{S}_{\hat{x}} = (\mathbf{K}^T \mathbf{S}_y^{-1} \mathbf{K} + \mathbf{S}_a^{-1})^{-1}. \quad (4)$$

For derivation see Rodgers (2000).

For multiple time steps, we chain the different atmospheric transport situations by concatenating the matrix  $\mathbf{K}$  for each time step  $t$  of  $t \in (t_1, \dots, t_n)$  and construct a forward model  $\mathbf{K}_T$  for all time steps, which can be separated into  $t_n$  independent sets of linear equations if no correlation between states is assumed. The matrices  $\mathbf{K}$  for each time step are on the diagonal of the new  
 145 matrix  $\mathbf{K}_T$  as the model GRAMM/GRAL assumes steady-state conditions. This means that the concentration field in an hour depends only on the emissions of the respective hour and not on the hours before. If the atmospheric transport changes from one hour to the next, so will the matrix  $\mathbf{K}$ .

$$\begin{pmatrix} y_0 \\ y_1 \\ \vdots \\ y_{t_n} \end{pmatrix} = \begin{pmatrix} \mathbf{K}_0 & \mathbf{0} & \dots & \mathbf{0} \\ \mathbf{0} & \mathbf{K}_1 & \dots & \mathbf{0} \\ \vdots & \vdots & \ddots & \vdots \\ \mathbf{0} & \mathbf{0} & \dots & \mathbf{K}_{t_n} \end{pmatrix} \cdot \begin{pmatrix} x_0 \\ x_1 \\ \vdots \\ x_{t_n} \end{pmatrix} = \mathbf{K}_T \cdot \begin{pmatrix} x_0 \\ x_1 \\ \vdots \\ x_{t_n} \end{pmatrix}. \quad (5)$$

This equations simplifies and the number of state vectors decreases, if a constant diurnal cycle of the emissions is assumed:

$$150 \quad \begin{pmatrix} y_0 \\ y_1 \\ \vdots \\ y_{23} \\ y_{24} \\ y_{25} \\ \vdots \\ y_{t_n} \end{pmatrix} = \begin{pmatrix} \mathbf{K}_0 & \mathbf{0} & \dots & \mathbf{0} \\ \mathbf{0} & \mathbf{K}_1 & \dots & \mathbf{0} \\ \vdots & \vdots & \ddots & \vdots \\ \mathbf{0} & \mathbf{0} & \dots & \mathbf{K}_{23} \\ \mathbf{K}_{24} & \mathbf{0} & \dots & \mathbf{0} \\ \mathbf{0} & \mathbf{K}_{25} & \dots & \mathbf{0} \\ \vdots & \vdots & \ddots & \vdots \\ \mathbf{0} & \mathbf{0} & \dots & \mathbf{K}_{t_n} \end{pmatrix} \cdot \begin{pmatrix} x_0 \\ x_1 \\ \vdots \\ x_{23} \end{pmatrix} = \mathbf{K}_T \cdot \begin{pmatrix} x_0 \\ x_1 \\ \vdots \\ x_{23} \end{pmatrix} \quad (6)$$

Solving for the posterior emissions  $\hat{x}$  requires the prior probability distribution, which is given as a multivariate Gaussian distribution defined by the vector of the mean values for each state  $x_a$  and the covariance matrix  $\mathbf{S}_a$ . In the case of uncorrelated states, the prior covariance matrix is  $\mathbf{S}_a = \text{diag}(\sigma_a^2)$  with the variances of the state  $\sigma_a^2$  on the diagonal. For correlated states, a common choice of correlation is an exponentially decaying correlation defined by a single parameter per dimension (Kunik  
 155 et al., 2019). The single parameter defines the strength of the correlation along a distance of a dimension. In principle, the

correlation in the prior reduces the total uncertainty of the prior and links the different hours of the inversion making the inverse problem numerically more complex at the same time. We analyse the influence of temporal correlation in the prior of fluxes in Sect. 3.4. The correlation is defined by a correlation strength  $\tau_t$  for the time difference between states at the same position. With that the covariance is

$$160 \quad \text{Cov}(\mathbf{x}_{i,t_0}, \mathbf{x}_{i,t_1}) = \sigma_{i,t_0} \sigma_{i,t_1} \exp\left(\frac{|t_1 - t_0|}{\tau_t}\right) \quad (7)$$

with the standard deviation of state  $x_i$  at time  $t_0$  and time  $t_1$  as  $\sigma_{i,t_0}$  and  $\sigma_{i,t_1}$  respectively.

In Sect. 3.3, we analyse the benefit of measuring CO additionally for estimating CO<sub>2</sub> emissions. We assume that they are both passive tracers and thus share the same forward model matrix  $\mathbf{K}$ . The CO<sub>2</sub> emissions can then be expressed in terms of the CO emissions as

$$165 \quad \begin{pmatrix} \mathbf{y}_{\text{CO}_2} \\ \mathbf{y}_{\text{CO}} \end{pmatrix} = \begin{pmatrix} \mathbf{K} & \mathbf{0} \\ \mathbf{0} & \mathbf{K} \end{pmatrix} \cdot \begin{pmatrix} \mathbf{x}_{\text{CO}_2} \\ \mathbf{x}_{\text{CO}} \end{pmatrix} = \begin{pmatrix} \mathbf{K} & \mathbf{0} \\ \mathbf{0} & \mathbf{K} \end{pmatrix} \cdot \begin{pmatrix} \mathbf{I}_n \\ \mathbf{A}_{\text{CO}} \end{pmatrix} \cdot \mathbf{x}_{\text{CO}_2} = \begin{pmatrix} \mathbf{K} \\ \mathbf{K}\mathbf{A}_{\text{CO}} \end{pmatrix} \cdot \mathbf{x}_{\text{CO}_2} \quad (8)$$

with  $\mathbf{A}_{\text{CO}}$  as a diagonal matrix with the flux-weighted mean emission factors  $\alpha_{\text{CO}}$  per sector with

$$\alpha_{\text{CO},i} = \frac{\sum_s x_{i,s} \alpha_{\text{CO},s}}{\sum_s \alpha_{\text{CO},s}} \quad (9)$$

with  $x_{i,s}$  as the CO<sub>2</sub> emissions of sector  $s$  in flux state vector entry  $i$  and  $\alpha_{\text{CO},s}$  as the emission factor for sector  $s$ .  $\sum_s$  is the sum over all sectors. We assume the emission factors to be exact for the optimization in the Bayesian inversion system.

## 170 2.3 Evaluation metrics

To describe the properties of the inversion and evaluate the set-ups of the OSSEs, we introduce evaluation metrics, namely the information content, the relative improvement and the root mean square error (RMSE). The metrics evaluate the quality of the inversion (result) and are sensitive to slightly different aspects of the evaluation. Some require the true emissions, while others are able to evaluate the quality of the inversion without knowing the truth. Further, the metrics differ in the computational costs.

175 For the analysis, we choose the metric that allows us to best analyse the system and highlight the impact.

First, the information content of the measurement can be derived from the concept of Shannon information, which is similar to the physical entropy (Rodgers, 2000). The Shannon information for the difference of prior and posterior probability for the Bayesian inversion in a linear case and given Gaussian probability distribution is:

$$H = -\frac{1}{2} \log(|\mathbf{S}_{\hat{x}} \mathbf{S}_a^{-1}|) = -\frac{1}{2} \log |\mathbf{I}_n - \mathbf{A}| \quad (10)$$

180  $\mathbf{A}$  denotes the averaging kernel and  $\mathbf{I}_n$  is the identity matrix with dimension  $n$ . For details on the concept and derivation see Rodgers (2000). One can see that the information content increases with the averaging kernel becoming close to identity. The

information content describes the quality of the set-up independently of the actual difference between prior and the truth. It can therefore be used as a measure for the quality of the inversion, in which the truth is not known. As it is a scalar quantity, it is useful for optimising observing systems, as well as characterising and comparing them.

185 However, in an OSSE, the truth is known, such that the difference between truth and posterior emissions can also be used for evaluation of the set-up. The RMSE over the entire domain is defined as the difference between the sum of the two vectors  $\hat{x}_{tot}$  and  $x_{tot}^*$ .

$$\text{RMSE}(\hat{\mathbf{x}}_{tot}, \mathbf{x}_{tot}^*) = \sqrt{\frac{1}{t_n} \sum_{t=0}^{t_n} (\hat{\mathbf{x}}_{tot,t} - \mathbf{x}_{tot,t}^*)^2} \quad (11)$$

The RMSE of the total fluxes gives quantitative information on how close the total posterior flux  $\hat{x}_{tot}$  is to the true total  $x_{tot}^*$  in the domain. In contrast to the information content, it does not capture the complete probability distribution, but rather the effect of the stochastically generated noise. However, it is computationally cheaper to calculate. Additionally, the relative improvement can be calculated, if the true emissions are known:

$$\eta = 1 - \frac{\|\hat{x} - x^*\|_2}{\|x_a - x^*\|_2} \quad (12)$$

with the prior flux  $x_a$ , the posterior flux  $\hat{x}$ , and the true emissions  $x^*$ . The relative improvement scales the difference between the posterior and the truth of each state by the difference between the prior and the truth of the states. The relative improvement is 0 % if the RMSE of the posterior has not improved compared to the prior and 100 % if the posterior and the truth are identical.

## 2.4 Emission data and uncertainties

In this study, we simulate anthropogenic CO<sub>2</sub> enhancements. In the following, we explain the data sets used to construct the true emissions as well as the prior for the inversion. The fluxes of the inventories have a high resolution (see Sect 2.4.1 and 200 2.4.2), but we group the fluxes into emission groups, which we use as basis vector for the inversion. The emission groups are administrative districts. Therefore, only the total emissions per administrative district is optimised for, even though a district still exhibits a higher resolved sub-structure. While there are actually 26 administrative districts, small districts and districts at the domain border have been aggregated (see Fig. C1) such that there are 19 districts, which can be optimized. The reason for choosing administrative districts is that the emission information should meet the needs of stakeholder (Jungmann et al., 2022) and should be well constrained by a reasonable number of sensors. For Heidelberg, administrative districts are a 205 politically meaningful unit exhibiting an area large enough to be constrained with a realistic number of sensor nodes. We chose to aggregate smaller districts and border districts as they are very difficult to constrain as they contribute only weakly to an overall enhancement. To assign area emissions on district level, area sources are interpolated to the GRAL grid of 10 m x 10 m and each pixel on the GRAL grid is assigned to the district with the maximum overlap.



## 210 2.4.1 True emissions

For the true emissions, we use data with a high spatial and temporal resolution to reflect the expected heterogeneity and variability of the emissions in the urban area. Traffic emissions were taken from a OpenStreetMap-based emission estimate (Ulrich et al., 2023) as line sources with street-resolving (3 m) resolution. Combustion emissions are based on data for the yearly consumption of natural gas, fuel, oil, liquid gas, coal, wood and pellets in the municipality of Heidelberg, as provided by the public utility company of Heidelberg ("Wärme Atlas 2017 Aggregation", version 001). The emissions are primarily caused by residential heating and do not include traffic emissions. The combustion data is aggregated on a grid with a resolution of 100 m x 100 m to protect the privacy of the customers. For the same reason, if there are less than five customers in a single grid cell, the data is masked and not available in the inventory. We treat masked emissions as if they do not contribute, i.e. set these grid cells to zero. Finally, the remaining emissions from Gridded Nomenclature for Reporting (GNFR) sector G to L are additionally accounted for as true emissions. We use the area emissions provided by TNO (Nederlandse Organisatie voor Toegepast Natuurwetenschappelijk Onderzoek) as true residual emissions. However, these area emissions contribute to only 1.4 % to total emissions (see Table 1). All true emissions are then cut into administrative districts for division into base vectors (see Fig. C1), but still have a sub-structure, as described above and as illustrated in Fig. 2.

There are only two TNO point sources in the GRAL domain which are treated each as individual group. The two TNO point sources in the domain are emitted as point sources at stack heights of 85 m and 120 m. A fixed diurnal and weekly cycle of emissions is assumed following the profiles listed for each GNFR sector by Van Der Gon et al. (2011).

## 2.4.2 Prior Emissions

We use emission data from the TNO inventory (Super et al., 2020) as starting point for constructing the prior. The data set consists of an inventory of area sources with a resolution of  $1/60^\circ$  longitude x  $1/120^\circ$  latitude ( $\approx 1$  km x 1 km over Central Europe) and point sources. TNO emissions are shown for the Heidelberg GRAL domain in Fig. B1. While the data set consists of ten different emission maps which were constructed with a Monte Carlo approach, only the first realization of the set is used. Emissions are divided into emission categories according to the GNFR category for both  $\text{CO}_2$  and CO. From this, the mean emission factor  $\text{CO}/\text{CO}_2$  for each GNFR category for the entire GRAL domain is obtained. The emissions and ratios for the Heidelberg domain are listed in Table 1 and are used in Sect. 2.4.

TNO area emissions are divided into administrative districts as described above. We further smooth out the area TNO emissions such that the mean emissions per area are equal for each district, however they are not constant over the domain as emissions per area still exhibit a sub-structure within the district (see Fig. 2). The prior emissions are set constant in time and do not have a diurnal cycle. The reason for introducing smoothing across districts, as well as the constant temporal profile for the prior is to reflect a realistic difference between prior and truth that would also be expected in a real inversion. In addition to the area sources, the TNO point sources are also accounted for in the prior.

The prior uncertainties for TNO point and area sources are set to 100 % of the prior flux. Prior uncertainties for traffic and combustion sources are set to 100 % of the true emissions as the prior emissions for traffic and combustion sources are zero.

**Table 1.** CO<sub>2</sub> and CO emissions per year in Heidelberg and ratio of CO/CO<sub>2</sub> [ppb ppm<sup>-1</sup>] for different Gridded Nomenclature for Reporting (GNFR) emission sectors as taken from TNO (Super et al., 2020). The ratio was calculated by converting from kg to parts per million (ppm) or parts per billion (ppb) by taking into account the molecular mass of CO and CO<sub>2</sub> and assuming standard conditions. The GNFR sectors are the basis for reporting spatially distributed emissions of air pollutants by European countries.

GNFR	Sector name	CO <sub>2</sub> emissions [kg a <sup>-1</sup> ]	CO emissions [kg a <sup>-1</sup> ]	CO/CO <sub>2</sub> [ppb ppm <sup>-1</sup> ]
A	Public Power	1.4e+08	2.8e+05	3
B	Industry	5.4e+08	9.6e+05	3
C	Other Stationary Combustion	3.5e+08	2.0e+06	9
D	Fugitives	0	0	nan
E	Solvents	5.5e+06	3.0e+04	9
F1	Road Transport gasoline	6.6e+07	1.1e+06	25
F2	Road transport diesel	1.2e+08	8.7e+04	1
F3	Road transport LPG	2.2e+06	6.8e+03	5
G	Shipping	7.4e+05	1.2e+03	3
H	Aviation	0	0	nan
I	OffRoad	6.6e+06	2.3e+05	56
J	Waste	0	1.8e+02	inf
L	Agriculture other	1.0e-07	0	0

In total, there are 59 emission groups consisting of two point sources, and 19 districts with emissions from the TNO area sources, the traffic simulations, and the combustion data. This choice of emission groups defines the dimension  $n$  of the inversion framework. Figure 2 illustrates the three emission groups (area, combustion and traffic) belonging to the district Weststadt. The temporal mean emission strength of all emission groups is illustrated in Fig. 3 for prior, prior uncertainty and truth, respectively.

Note the differences between the magnitude of the emission groups in prior and truth. As prior and true emissions are accounted for in different emission groups, corresponding to different vector entries in state  $x$ , the inversion needs to redistribute to the other source types to correctly estimate sectoral and spatial patterns. This configuration pushes the limits of the current inversion set-up as it tests the capabilities of the inversion system to identify spatially overlapping emission groups. For the entire domain, prior and true emissions differ in average by 13.5%  $((\text{truth-prior})/\text{truth})$ .

## 2.5 The inversion experiments

This study examines the performance and design parameters of a network of sensors that measure the CO<sub>2</sub> concentration in air in an urban environment by combining a high-resolution atmospheric transport model on building-resolving scale with an atmospheric inverse model. The investigation focuses on various aspects to gain initial insights into the capabilities of a monitoring network in Heidelberg. To systematically analyse different parameters of a measurement network, we conduct

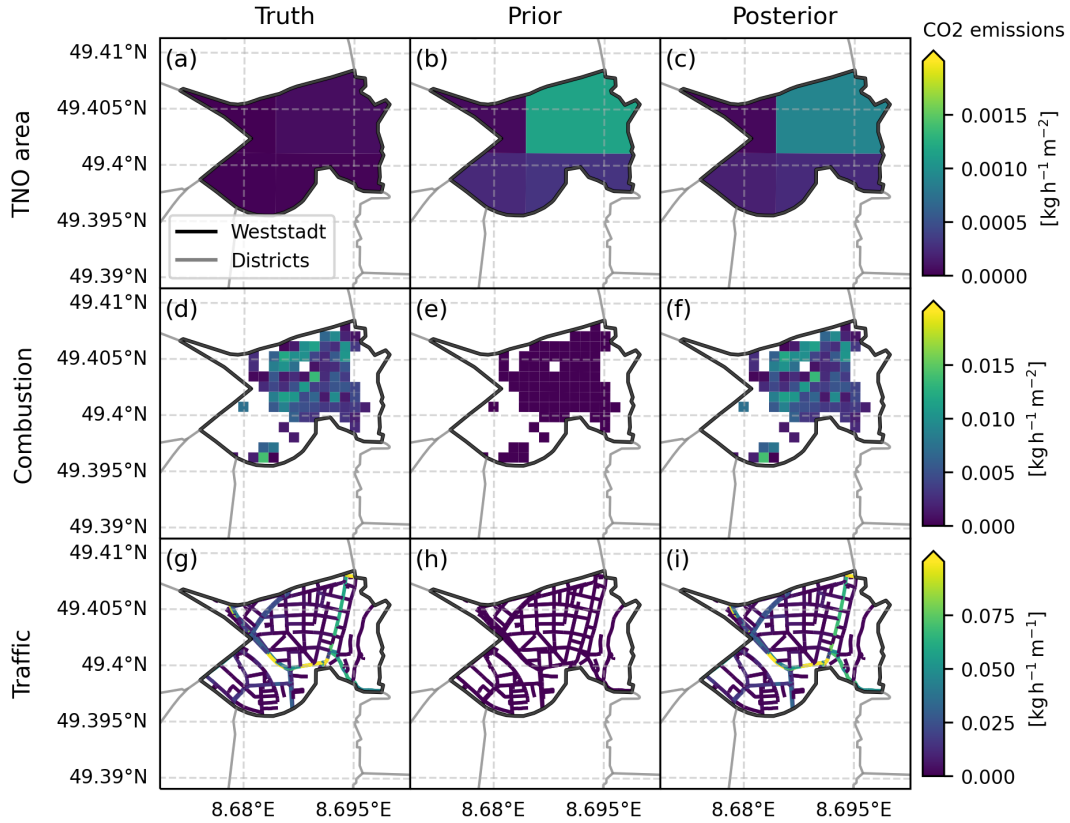


**Figure 2.** For the city district Weststadt ("We") three elements of the state vector are shown (three rows). The columns show the true, prior and posterior emissions for TNO area emissions (upper row), combustion emissions (middle row) and traffic emissions (lower row). This plot illustrates three of the state entries seen in Fig. 3. Note, that the prior (middle column) for combustion and traffic is zero, but exhibits the fixed substructure of the truth. The combustion emission in the district exhibits white 100 m x 100 m squares, which are masked due to data protection policy. The posterior emissions differ depending on the data assimilated and are illustrated here for 10 CO<sub>2</sub> measurements in the entire Heidelberg domain with 1 ppm uncertainty. Posterior results will be discussed in Sect. 3.

four separate experiments, each targeting different aspects of network design or inversion set-up. We analyse the number of sensors vs. the quality of sensors (Sect.3.1), the optimal horizontal sensor placement (Sect. 3.2), the benefit of utilising CO<sub>2</sub> as additional tracer (Sect. 3.3) and the effect of introducing a temporal correlation in the prior error covariance (Sect. 3.4). In all experiments, the virtual sensors, which "sample" the atmospheric trace gas concentrations are placed at 2 m above ground level and positioned such that they form a rectangular grid that covers the domain. Then, either all sensors are used or they

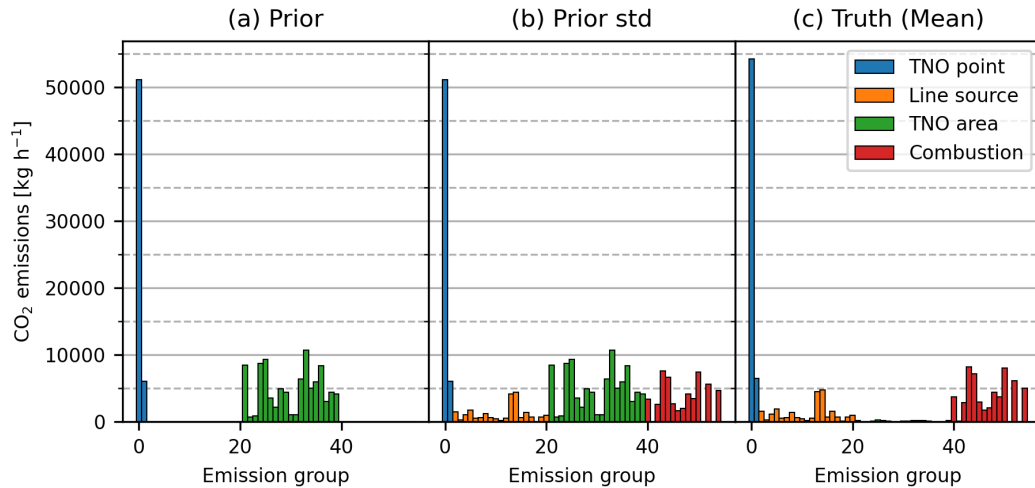


**Figure 3.** Emissions of each state vector for prior (left), uncertainty of the prior (middle) and truth averaged over time (right). The different emission groups contain emissions from the TNO point (blue) and area sources (green), the traffic simulations (orange), and the combustion sources (red).

are sub-sampled from the grid as described for each respective experiment in Sect. 3. The grid is chosen as a first approach to find the optimal sensor placement. The inversions are performed for wind situations during the period of 22.07.2021 to 21.08.2021. For the experiments in Sect. 3.1 - 3.2, 24 random hours are sampled from the first 300 hours of the period. For the experiments in Sect. 3.3 - 3.4, the first consecutive 120 hours (5 days) of the period are used for the inversion to test if the posterior estimate captures the correct temporal pattern. For the inversion, we assume constant emissions in Sect. 3.1 - 3.2 and a fixed diurnal cycle as described in Sect. 2.4 for Sect. 3.3 - 3.4. In the conducted OSSE, the influence of biogenic CO<sub>2</sub> fluxes and background concentrations is not considered. Instead, the simulated concentration fields specifically represent the increase in CO<sub>2</sub> concentration resulting from anthropogenic fluxes within the domain. This simplification corresponds to periods when biogenic influences in the city center are very small, most likely in winter, and exact background estimations of CO<sub>2</sub> transported from out of the domain into the domain are available. Both assumptions are not valid during most parts of the year. However, the goal of this OSSE is to evaluate the inversion framework and analyse the sensitivity of network configurations to CO<sub>2</sub> emission estimates as starting point for optimal network design in Heidelberg. As such, we do not claim completeness. We elaborate on the limitation caused by these simplifications in Sect. 4.

### 3 Results

#### 3.1 Sensor quality and quantity

The optimal design of a measurement network is constrained by the total costs of the network limiting quantity and/or quality of the used sensors and transport model. In this experiment, the quality of the inversion is investigated for different numbers of sensors with different mismatch errors  $S_y$ . The mismatch error includes instrument errors, model errors as well as representation errors. While all of the errors are inevitable, the instrument errors deserve special focus as it is a design variable for building a monitoring network. High cost sensors have better precision than mid-cost or low cost sensors, but are much more expensive such that we expect a trade-off between quality and quantity for a given budget. We follow the set-up by Turner et al. (2016) and conduct multiple Monte Carlo experiments each with  $N = 2000$  runs. In a Monte Carlo experiment a model variable, in our case sensor location, is sampled randomly to estimate the probability of having a certain outcome, in our case of having a certain information content of the inversion. We place 5, 10, 15, 20, 25 and 30 sensors randomly on a 5 x 6 grid within the domain (30 possible locations) with a total noise of 0.1, 0.5, 1.0, 2.0, 3.0, 4.0, 5.0, 10.0 ppm. We conduct the analysis for 24 randomly selected wind situations. For illustration purposes, Fig. 2 plots the true (left column), prior (middle column) and posterior emissions (right column) for the district "Weststadt" on a map for the three emission groups, namely for area emissions (upper panel), combustion emission (middle panel) and traffic emissions (lower panel). One can see that an emission group is not flat, but exhibits a substructure. Posterior emissions are shown for a specific setting (10 CO<sub>2</sub> measurements with 1 ppm uncertainty). The mean posterior result for each state (all districts, all sectors, same setting) can be seen left in Fig. 4.

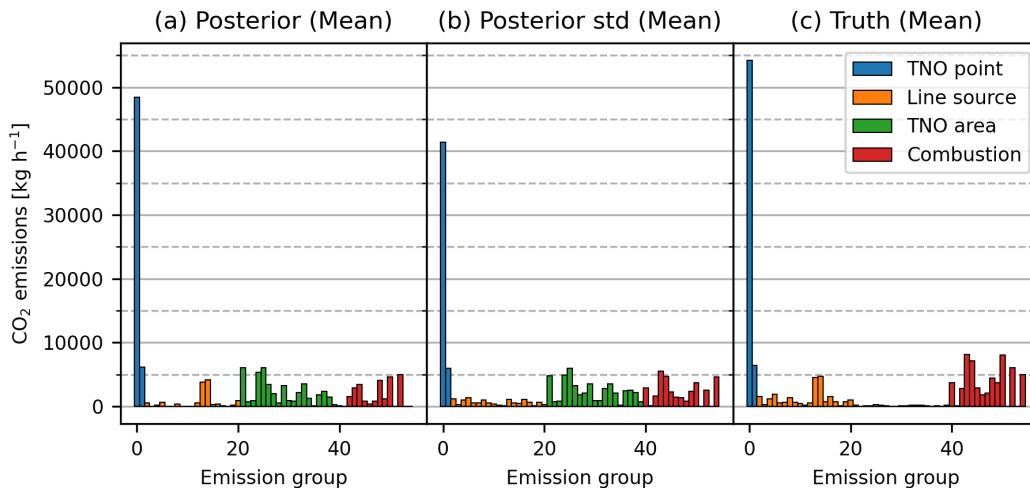


**Figure 4.** Left: Mean posterior emissions of each state vector. Middle: Mean posterior uncertainty. Right: True emissions of each state vector. The different states refer to emissions from the TNO point (blue) and area sources (green), the traffic simulations (orange), and the combustion sources (red). Note that the prior emissions and uncertainties are given in Fig. 3.

For quantitative analysis of the optimal configuration, Fig. 5 shows the relative improvement of the estimation of the city-wide emission flux for the different sensor noises and number of sensors. The relative improvement increases with quantity and with decrease of model-data mismatch error, e.g. by increasing the quality of sensors. Similar to Turner et al. (2016), we can identify noise-limited configurations (e.g. 25 sensors at 2 ppm uncertainty in Fig. 5) for which the flux estimation improves more by increasing the quality of the sensors and models and site-limited (e.g. 5 sensors at 2 ppm uncertainty in Fig. 5) where the flux estimation improves more by increasing the number of sensors. While the quality of flux estimation increases with number of sensors and sensor quality, the budget for a sensor network is limited. The best choice of network depends on the monetary constraints for the sensor network and the costs of each sensor.

The plot allows comparing the relative improvement of flux estimation for different networks in Heidelberg. One can then utilize Fig. 5 to identify the configurations that are still affordable (subset of squares in Fig. 5) and find the configuration that maximises the relative improvement of the flux estimation. This implies, that for any given budget, one can base a decision on investing in more or in better sensors (and models) on these results. Note that we here only account for a random uncertainty in sensor noise assuming uncorrelated measurement uncertainties among sensors. We do not analyse systematic errors within the measurement network, which could be present because of e.g. temperature dependent drifts of the sensors (Delaria et al., 2021) or by a background transport errors. While analyzing systematic offsets was not the scope of this study, the established inverse framework can be easily used to study such effects in future.

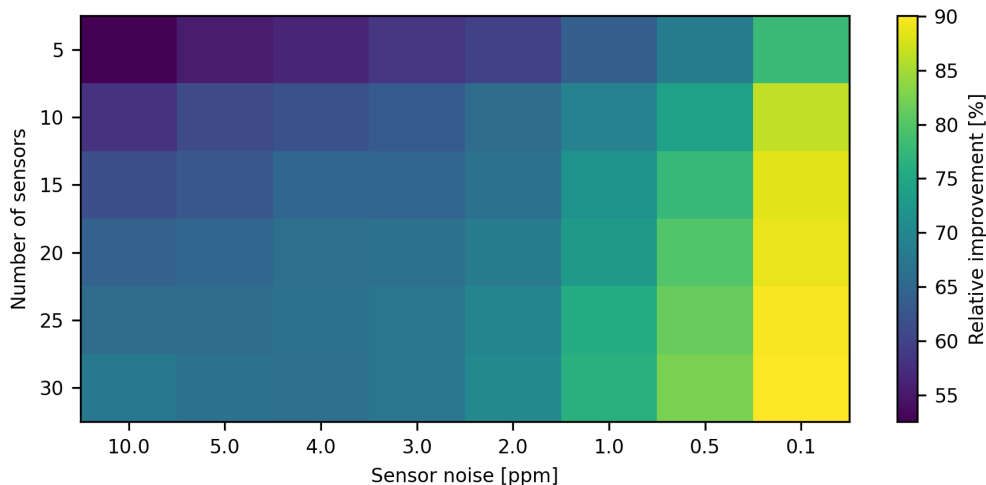


**Figure 5.** Relative improvement of estimate for different configurations of the number of sensors and the measurement error of the sensors. The relative improvement increases with increasing number of sensors and sensor noise.

## 3.2 Sensor placement

310 In Sect. 3.1 we have randomly sub-sampled a number of sensors from a  $5 \times 6$  grid. Now, we analyse the optimal spatial distribution of the sensors. We therefore compare the sensor placement in a regular grid to randomly selecting locations in the domain. For the random selection, we run Monte Carlo simulations (each  $N=2000$ ) for different sensor numbers again using 24 randomly selected wind situations and offering 100 ( $10 \times 10$  grid) different possible sensor positions at 2 m above ground. We analyse the information content, for 9, 16, and 25 sensors for the random placement and for a regular grid placement

315 assuming a measurement precision of 1 ppm (see Fig. 6). One can clearly see that the information content increases with the number of sensors, as expected as more sensors better inform on the emissions. On average, the grid placement outperforms the random placement as can be seen from the mean values in Fig. 6. This means that without further information on the underlying emission statistics, it is beneficial to place the sensors in a regular grid rather than placing them randomly. This is expected as a regular grid covers the entire domain and therefore is less likely to be insensitive to emissions from specific

320 areas. The difference between random and grid placement, as well as the distribution of the random placement, is especially large for a small number of sensors. For a low number of sensors, the random placement of sensors is more likely to be spatially heterogeneous and therefore may be especially well or bad placed contributing to lower and higher information content as in the random placement. The distribution of information content for the randomly placed sensors decreases for higher number of sensors due to a better statistic. Interestingly, the placements with the highest information content are again

325 random placements. We analysed the right tail (10 best performing sensor arrangements) of the random distribution of nine sensors with high information content. Figure 7 shows the locations of the configurations with the highest information content. The locations with large incident number produce a large information content in many meteorological situations and should therefore be considered as optimal location for a measurement network. As the tail of the distribution corresponds to individual realizations of the Monte Carlo experiments, it remains unclear whether the “high information content tail” is driven by a

330 specific set of wind situations or if these measurement locations outperform the grid placement in all wind situations. For our Heidelberg setting, one can see that the measurement locations providing most information content are located in the city center and in vicinity to higher emissions. In the East of the domain, which is dominated by forest areas with low anthropogenic  $\text{CO}_2$  emission in the true emissions, only few sensors are placed. In future, we plan to extend this study by considering also measurement stations at higher altitudes above ground as higher stations are less influenced by local sources and are therefore

335 likely to provide information on the emission patterns over a larger area. This might be complementary to the ground-based sensors.

## 3.3 CO as additional tracer

CO is co-emitted when burning fossil fuels. Depending on the source type, the  $\text{CO}/\text{CO}_2$  ratio of the emissions differs (see Table 1). As CO and  $\text{CO}_2$  are nearly passive during an hour, both tracers are transported linearly with the same atmospheric transport.

340 Therefore, measuring the atmospheric CO concentration can provide additional information about the specific emission groups and potentially also about the total  $\text{CO}_2$  emissions in general as both stem from anthropogenic sources. We now analyse

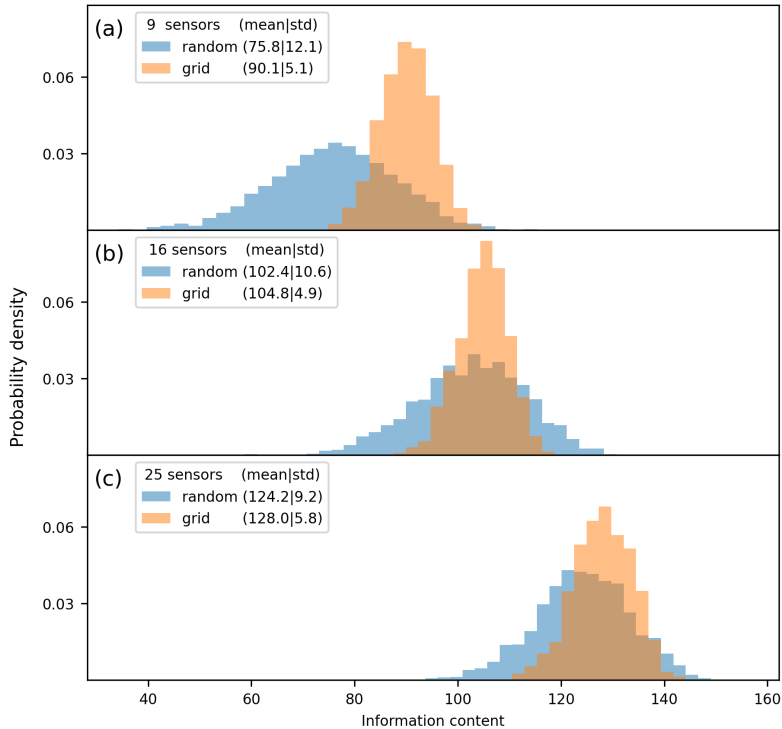


**Figure 6.** Information content distribution for the inversion set-up for varying wind conditions. The information content increases with number of sensors. The mean information content of randomly placed sensors (blue) is larger in the grid placement, but as the standard deviation of the random placement is larger, the highest information content is achieved for some configurations with randomly placed sensors.

to which degree the estimation of  $\text{CO}_2$  emissions benefits from measuring CO enhancement as additional tracer along with  $\text{CO}_2$ . Note, that we neglect biogenic CO emissions, which are normally expected to be much smaller than anthropogenic CO emissions in cities. While the mean  $\text{CO}/\text{CO}_2$  ratio of all anthropogenic sources in Heidelberg is  $5 \text{ ppb ppm}^{-1}$ , it is about  
 345  $9 \text{ ppb ppm}^{-1}$  for traffic emissions (see GNFR sectors f1-F3 in Table 1) making CO measurements especially sensitive to traffic emissions.

In this experiment, we assume that all measurement stations measure both  $\text{CO}_2$  and CO with uncorrelated measurement errors of  $1.0 \text{ ppm}$  for  $\text{CO}_2$  and  $2.0 \text{ ppb}$  for CO. The inversions are performed for a period of 5 days and the diurnal cycle is assumed to be identical for each day. We conduct this experiment using 10 sensors. The prior is constant during the period and  
 350 we do not introduce any correlation into the prior.

Figure 8a shows the total anthropogenic  $\text{CO}_2$  emissions during the course of the day. While the prior is constant in time, the truth actually shows a temporal profile with distinct morning peak. One can see that both inversion results (posterior with  $\text{CO}_2$  only and with  $\text{CO}_2$  and CO) differ from the flat prior and are able to capture the profile of the true total emissions. In the



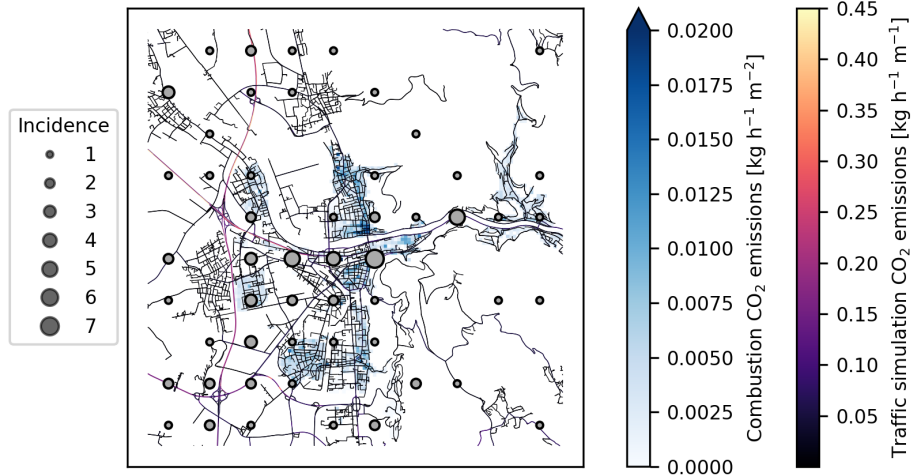


**Figure 7.** Sensor positions of the 9 sensors with the 10 largest information content. The size of the dots indicates the incidence of the sensor position of the 100 available positions in the experiment.

given setting, there is no significant improvement of the posterior emissions of total  $\text{CO}_2$  when including CO in the inversion. Note that this finding only holds in our setting when neglecting biogenic emissions. However, for future studies, we encourage re-analysing the benefit of CO for total anthropogenic  $\text{CO}_2$  when including biogenic emissions. Figure 8b shows the traffic emissions. Again, both posterior inversions differ from the flat prior emissions. However, the posterior estimate using the CO as additional constraint in the inversion is much closer to the true emissions. The same is true for combustion emissions (see Fig. 8c). This means that in our setting, for the given emission ratios and measurement uncertainties, the additional measurement of CO is useful in the inversion to separate different emission groups.

### 3.4 Temporal correlation of the prior

In the previous sections, we have retrieved the  $\text{CO}_2$  emissions for every hour without assuming any correlation between the states. Without temporal correlation, each hour of the inversion is independent of the previous and the following hour. We now examine the effect of considering temporally correlated states to reflect the existence of temporal emission trends exceeding 1 hour time scales. A correlation in the prior reduces the total uncertainty of the prior. However, the choice of the correct correlation length is vital. A larger correlation length leads to a smoothed time series as measurements inform multiple emission states and thus exhibit a larger corrective power over neighbouring hours. On the other hand, smaller correlation lengths can better account for spikes during the measurements. The choice of optimal correlation length therefore depends on the underlying emission patterns.

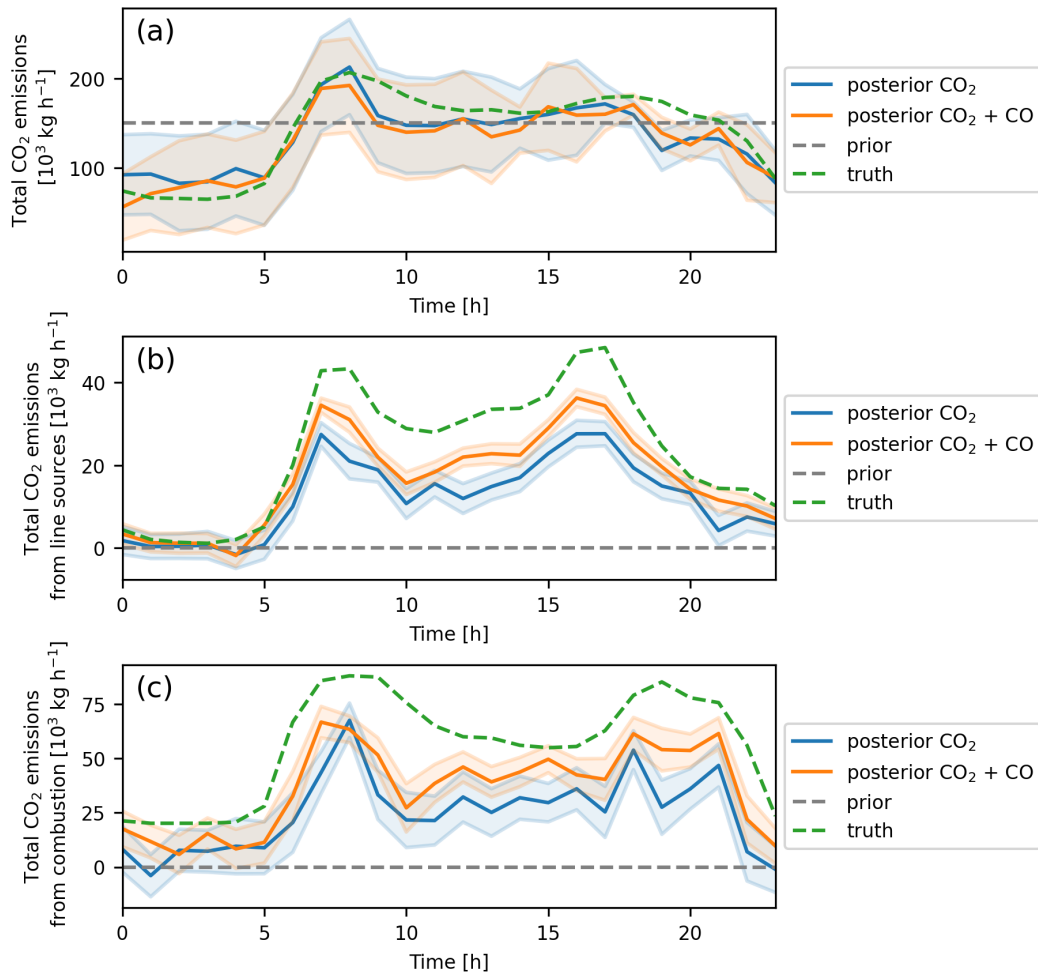


**Figure 8.** a) Diurnal cycle of the total CO<sub>2</sub> emissions in Heidelberg. The figure shows the posterior for an inversion utilising CO<sub>2</sub> only (blue) and an inversion utilising CO<sub>2</sub> and CO (orange). The shaded area is the standard deviation derived from the posterior covariance. The dotted lines show the prior emissions (gray) and the truth (green). b) Same as a, but for traffic instead of total CO<sub>2</sub> emissions. c) Same as a, but for combustion emissions.

370 In a first analysis, we have varied the correlation length  $\tau_h$  and analysed how the RMSE of the CO<sub>2</sub> emissions for different emission groups change with correlation length (see Fig. 9). This analysis is only possible in an OSSE when the truth is known and a RMSE can actually be determined.

As the optimal correlation length depends on the temporal emission dynamics, it is dependent on the source type. Focusing on the total CO<sub>2</sub> emissions, we find a clear minimum for about 2 hours. It is driven by a shorter optimal correlation length for point sources and longer optimal correlation lengths for traffic, heating or other area emissions. The curve for the point sources, which are emitted at heights of 85 m and 120 m, is qualitatively different from the curve of the ground-based sources. While  
 375

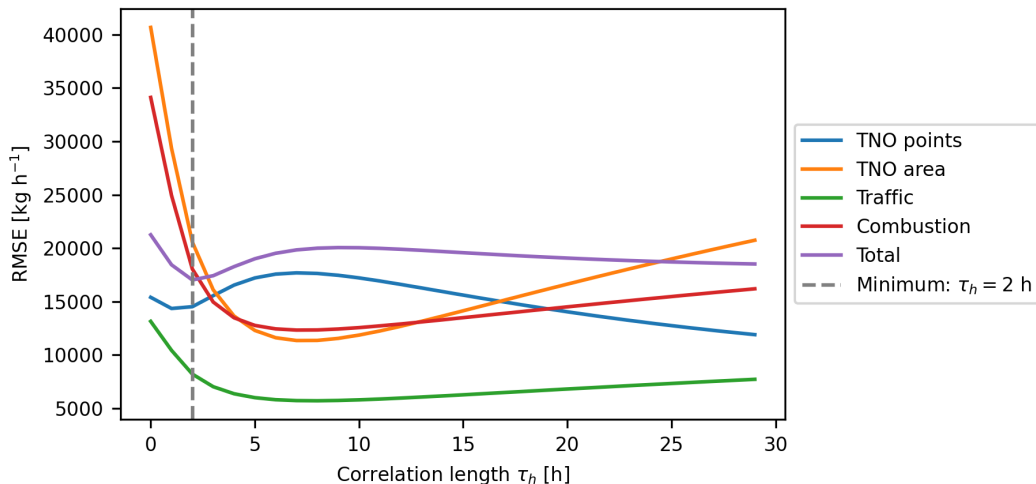


**Figure 9.** RMSE of the different emission sources for different correlation lengths  $\tau_h$ . The dashed gray line indicates the minimum of the RMSE for the total emissions, which is at a correlation length of 2 hours.

introducing any correlation time has a positive effect on the RMSE for ground-based sources, the effect can be detrimental for point sources. For point sources, correlation times between 4 and 15 hours are too strong for our setting. We here chose the 2 hours as correlation strength to estimate posterior emissions and highlight the importance of choosing the optimal correlation time especially for determining point sources. In Fig. 10a we analyse the benefit of using a posterior correlation of 2 hours to estimate total CO<sub>2</sub> emissions. The estimation of total CO<sub>2</sub> emissions improves when introducing the prior correlation. While the benefit is only small for total CO<sub>2</sub> emissions, the traffic and combustion emissions improve substantially when introducing a prior correlation (see Fig. 10b and c). This finding for our OSSE in Heidelberg is in accordance with the results from Kunik et al. (2019) in Salt Lake City. It shows that it is beneficial to introduce a temporal correlation of the prior states if underlying emission dynamics are temporally correlated as neighbouring states can inform and correct for each other.

#### 4 Discussion

In this set of experiments, we analyse the trade-offs inherent in balancing sensor quantity and sensor quality, we determine the optimal sensor locations, and evaluate the advantages of measuring CO, along with the impact of introducing temporal correlation into the inversion framework. These investigations are conducted within a simplified urban setting in Heidelberg.

The information content and, consequently, the precision of emission estimates depend on both the quantity and quality of deployed sensors. The potential accuracy of flux estimation increases with an increased financial budget, enabling the installation of additional or superior sensors. Through our experiments, we are able to determine the optimal sensor configuration—considering both quantity and quality—tailored to any given financial constraint.

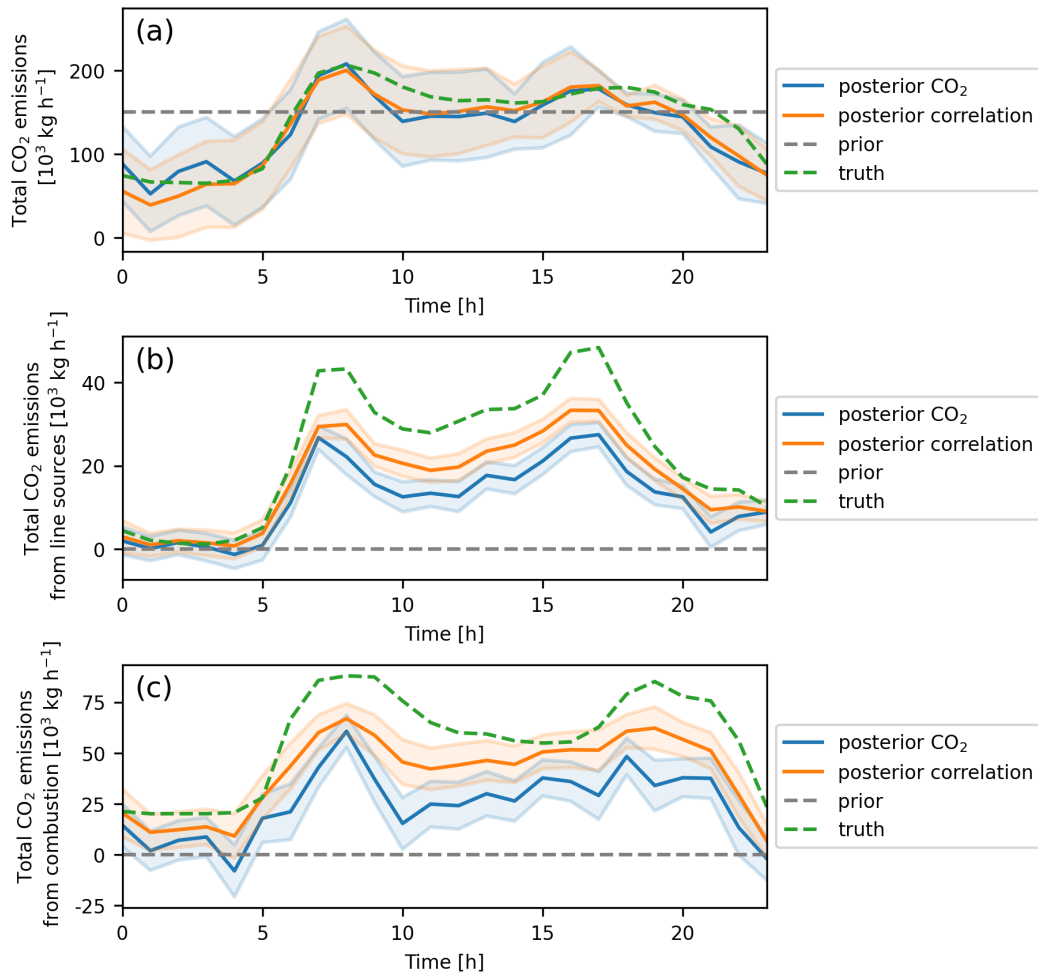


**Figure 10.** a.) Diurnal cycle of the total CO<sub>2</sub> emissions. The figure shows the posterior for an inversion with uncorrelated prior emissions (blue) and with time correlated prior emissions with a correlation length of two hours (orange). The shaded area is the standard deviation derived from the posterior covariance. The dotted lines show the prior emissions (gray) and the truth (green). b.) Same as a, but for traffic instead of total CO<sub>2</sub> emissions. c.) Same as a, but for combustion CO<sub>2</sub> emissions instead of total CO<sub>2</sub> emissions.

The experiments further suggest locations of preferred sensor installation based on Monte Carlo simulations. The GRAM-  
 395 M/GRAL model proves especially advantageous for assessing optimal sensor positions due to the storage of full concentration fields for each wind situation. Other models often compute footprints for predefined sites, which makes the analysis of a large number of possible sensor locations less efficient. We analyse the performance of a network with equally spaced sensors versus randomly placed sensors inside the domain. On average, equally spaced sensors outperform randomly placed sensors. This means that in absence of information on the emission distribution an equally spaced sensor placement is a good starting point.

400 However, there are network configurations that yield better performance in terms of emission estimates, particularly when located near emission sources and in the center of the domain.

Moreover, we assess the advantages of incorporating CO as an additional tracer. Although CO measurements do not significantly enhance the overall estimation of total CO<sub>2</sub> emissions in this setting, they do contribute to an improved estimation of sector-specific emissions. The limited impact of including CO for the estimation of total CO<sub>2</sub> emissions can be attributed to the  
405 absence of biogenic emissions in the presented setting. Consequently, the total CO<sub>2</sub> emissions are already well-represented by sampling the total simulated CO<sub>2</sub> enhancements. In reality, the total CO<sub>2</sub> enhancement, in contrast to total CO enhancement, is significantly influenced by biogenic sources – especially in spring and summer. Reassessing the benefit of CO as tracer for anthropogenic CO<sub>2</sub> is therefore encouraged after including biogenic emissions into the framework. Beyond that, it is possible to adjust CO/CO<sub>2</sub> ratios of different sectors to mimick anticipated changes in CO/CO<sub>2</sub> ratios, and evaluate the benefit of the  
410 tracers under these circumstances again.

Finally, we analyse the influence of the prior probability distribution on the inversion by introducing a temporal correlation in the prior emission estimate. The introduction of temporal correlation increases the overall uncertainty reduction. The optimal correlation length is source dependent, but is 2 hours for the total emissions in our setting. Using this correlation length improves the emission estimate and minimises the discrepancy between the posterior emission estimate and the true emissions,  
415 which again is in line with previous studies.

The results provide a first indication on how to construct a network and beyond that they show the principle applicability of GRAMM/GRAL in an inversion framework. However, all results still exhibit uncertainties due to various aspects: First, as any model, GRAMM/GRAL exhibits transport errors. The performance of GRAMM/GRAL has been assessed in multiple studies and has to be taken into account in the inversion (as model-data mismatch). Utilizing a wrong error for the model transport may  
420 distort the outcome of the inversion. The same argumentation holds for instrumentation errors. So far, we have only considered random noise for the model-data mismatch. However, the framework allows evaluating systematic biases, e.g. due to sensor drifts or emissions transported from out of the model domain to the sensor locations.

Second, introducing biogenic emissions and analyzing the effect of background concentrations is essential for drawing final conclusions on the design of the measurement network in urban areas. Biogenic emissions enhance the total CO<sub>2</sub> signal and  
425 thus mask the contributions from anthropogenic sources. The effect of transported CO<sub>2</sub> into the model domain will be larger the smaller the domain. In Heidelberg, we expect the effect of transported emissions to be considerable as emissions from the city of Mannheim influence the concentrations in Heidelberg for typical westwind situations. The magnitude of concentration enhancement and its effect on the emission estimation still needs to be explored in future. However, there are possibilities to account for the transported emissions – either by setting up dedicated measurement stations at the domain borders or by  
430 including an uncertainty for the background enhancement into the inversion framework, which will be explored in a next generation OSSE for Heidelberg.

Third, the choice of state vector will influence the result. In future, one might consider changing from emissions grouped into districts with fixed sub-district variation to e.g. a high-resolution regular grid. This would decrease the aggregation error

and account for finer spatial dynamics. However, as this increases the dimension of the state vector, more measurements will  
435 be necessary to determine the fluxes on higher resolution equally well.

While an OSSE will never be able to mimick the real world fully, approaching realistic setting in the model world is important to obtain the correct indications for sensor network planning. Using the presented framework, we can now add further complexity and conduct numerous additional experiments, such as exploring moving sensors, incorporating additional tracers, analyzing different sensor heights and extending to longer time periods.

## 440 **5 Conclusions**

We have developed a framework for conducting OSSEs using the high-resolution transport model GRAMM/GRAL. This framework allows to perform various experiments to assess the capabilities and sensitivity of a measurement network to specific parameters.

The developed framework represents a first step towards conducting atmospheric inversions using a transport model with  
445 a resolution much below the kilometer scale. The experiments allow comparing different network parameters and therefore optimising the network design based on high-resolution transport. We have demonstrated the feasibility of estimating CO<sub>2</sub> emissions for Heidelberg at a district level and give first indications for sensor network design. The main advantage of using GRAMM/GRAL in the inversion lies in the cost-effective forward model employed in the catalogue approach, as well as the assumption of hourly steady state in the model. This steady state assumption enables easy determination of the Jacobian re-  
450 quired for inversion. This advantageous characteristic facilitates network optimization across various parameters and locations, even encompassing areas influenced by street channeling and buildings. This framework provides the basis to efficiently estimate high-resolution CO<sub>2</sub> fluxes in an urban setting. In a next step, we can now further enhance the realism of the OSSE by incorporating additional complexities.

Code and data availability. The inversion code can be found at <https://doi.org/10.5281/zenodo.8354902> and <https://github.com/ATMO-IUP-UHEI/BayesInverse/tree/v.1.1>. Code to read and process GRAMM/GRAL output: <https://github.com/ATMO-IUP-UHEI/GGpyManager> and <https://zenodo.org/record/8375169>. Code to conduct the experiments: <https://github.com/ATMO-IUP-UHEI/Experiments> Forward modelled concentration data has been simulated using GRAMM/GRAL v19.1 (<https://github.com/GralDispersionModel>) and is archived on heiData: <https://doi.org/10.11588/data/NHIVDO>

## Appendix A: Abbreviations

**Table A1.** List of abbreviations used in the manuscript.

Abbreviation	Full name
CO	Carbon monoxide
CO <sub>2</sub>	Carbon dioxide
GNFR	Gridded Nomenclature For Reporting
GRAL	Graz Langrangian Model
GRAMM	Graz Mesoscale Model
OSSE	Observing System Simulation Experiment
ppb	parts per billion
ppm	parts per million
TNO	Nederlandse Organisatie voor Toegepast Natuurwetenschappelijk Onderzoek
RANS	Reynolds Averaged Navier Stokes
RMSE	Root Mean Square Error

## 460 Appendix B: Emissions

### B1 Prior emissions

### Appendix C: Districts chosen as state vectors for the inversion

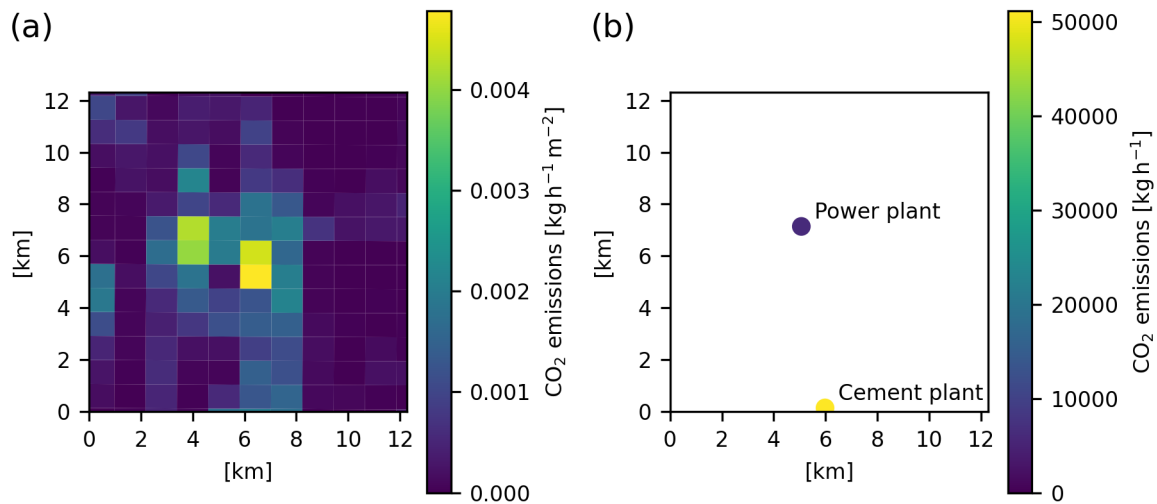


**Figure B1.** a.): TNO area emissions, b.): TNO point emissions for the GRAL domain in Heidelberg. Data is taken from Super et al. (2020).

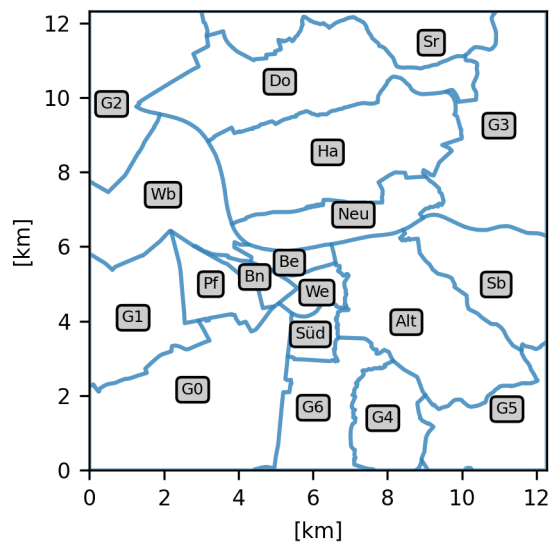


**Figure C1.** a) The districts used as states for the inversion. The full names as well as the administrative districts inside each district are listed in table C1.



**Table C1.** Overview over the district names and the administrative districts they represent. Smaller districts or district fragments are grouped together.

Code	Districts	Name
Alt	Altstadt	
Bn	Bahnstadt	
Be	Bergheim	
Do	Dossenheim	
Ha	Handschuhsheim	
Neu	Neuenheim	
Pf	Pfaffengrund	
Sb	Schlierbach	
Sr	Schriesheim	
Süd	Südstadt	
We	Weststadt	
Wb	Wieblingen	
G0	Oftersheim, Kirchheim, Sandhausen	Group 0
G1	Eppelheim, Plankstadt	Group 1
G2	Edingen-Neckarhausen, Ladenburg	Group 2
G3	Schönau, Ziegelhausen, Wilhelmsfeld, Weinheim	Group 3
G4	Emmertsgrund, Boxberg	Group 4
G5	Gaiberg, Bammental, Neckargemünd	Group 5
G6	Leimen, Rohrbach	Group 6

*Author contributions.* S.N.V conceptualised the experiments, set up the simulations, supervised the work and wrote the the original draft together with R.M. R.M. carried out the formal analysis, performed the simulations and developed the software code.

465 *Competing interests.* The authors declare no competing interests.

*Acknowledgements.* We thank André Butz for valuable discussions on experimental design and results. We thank Christopher Lueken-Winkels for helpful comments on the final draft. This research was partly funded by the German Research Foundation (DFG) within the Excellence Strategy, ExU 5.2 as granted by the Heidelberg Center for the Environment.

## References

- 470 Balashov, N. V., Davis, K. J., Miles, N. L., Lauvaux, T., Richardson, S. J., Barkley, Z. R., and Bonin, T. A.: Background heterogeneity and other uncertainties in estimating urban methane flux: results from the Indianapolis Flux Experiment (INFLUX), *Atmospheric Chemistry and Physics*, 20, 4545–4559, <https://doi.org/10.5194/acp-20-4545-2020>, publisher: Copernicus GmbH, 2020.
- Berchet, A., Zink, K., Muller, C., Oetl, D., Brunner, J., Emmenegger, L., and Brunner, D.: A cost-effective method for simulating city-wide air flow and pollutant dispersion at building resolving scale, *Atmospheric Environment*, 158, 181–196, <https://doi.org/10.1016/j.atmosenv.2017.03.030>, publisher: Elsevier Ltd, 2017a.
- 475 Berchet, A., Zink, K., Oetl, D., Brunner, J., Emmenegger, L., and Brunner, D.: Evaluation of high-resolution GRAMM–GRAL (v15.12/v14.8) NO<sub>x</sub> simulations over the city of Zürich, Switzerland, *Geoscientific Model Development*, 10, 3441–3459, <https://doi.org/10.5194/gmd-10-3441-2017>, 2017b.
- Blocken, B.: LES over RANS in building simulation for outdoor and indoor applications: A foregone conclusion?, *Building Simulation*, 11, 821–870, <https://doi.org/10.1007/s12273-018-0459-3>, 2018.
- 480 Bréon, F. M., Broquet, G., Puygrenier, V., Chevallier, F., Xueref-Remy, I., Ramonet, M., Dieudonné, E., Lopez, M., Schmidt, M., Perrussel, O., and Ciais, P.: An attempt at estimating Paris area CO<sub>2</sub> emissions from atmospheric concentration measurements, *Atmospheric Chemistry and Physics*, 15, 1707–1724, <https://doi.org/10.5194/acp-15-1707-2015>, 2015.
- Davis, K. J., Deng, A., Lauvaux, T., Miles, N. L., Richardson, S. J., Sarmiento, D. P., Gurney, K. R., Hardesty, R. M., Bonin, T. A., Brewer, W. A., Lamb, B. K., Shepson, P. B., Harvey, R. M., Cambaliza, M. O., Sweeney, C., Turnbull, J. C., Whetstone, J., and Karion, A.: The Indianapolis Flux Experiment (INFLUX): A test-bed for developing urban greenhouse gas emission measurements, *Elementa: Science of the Anthropocene*, 5, 21, <https://doi.org/10.1525/elementa.188>, 2017.
- 485 Delaria, E. R., Kim, J., Fitzmaurice, H. L., Newman, C., Wooldridge, P. J., Worthington, K., and Cohen, R. C.: The Berkeley Environmental Air-quality and CO<sub>2</sub> Network: field calibrations of sensor temperature dependence and assessment of network scale CO<sub>2</sub> accuracy, *Atmospheric Measurement Techniques*, 14, 5487–5500, <https://doi.org/10.5194/amt-14-5487-2021>, publisher: Copernicus GmbH, 2021.
- Deng, A., Lauvaux, T., Davis, K. J., Gaudet, B. J., Miles, N., Richardson, S. J., Wu, K., Sarmiento, D. P., Hardesty, R. M., Bonin, T. A., Brewer, W. A., and Gurney, K. R.: Toward reduced transport errors in a high resolution urban CO<sub>2</sub> inversion system, *Elementa: Science of the Anthropocene*, 5, 20, <https://doi.org/10.1525/elementa.133>, 2017.
- Jungmann, M., Vardag, S. N., Kutzner, F., Keppler, F., Schmidt, M., Aeschbach, N., Gerhard, U., Zipf, A., Lautenbach, S., Siegmund, A., Goeschl, T., and Butz, A.: Zooming-in for climate action—hyperlocal greenhouse gas data for mitigation action?, *Climate Action*, 1, 8, <https://doi.org/10.1007/s44168-022-00007-4>, 2022.
- 495 Kunik, L., Mallia, D. V., Gurney, K. R., Mendoza, D. L., Oda, T., and Lin, J. C.: Bayesian inverse estimation of urban CO<sub>2</sub> emissions: Results from a synthetic data simulation over Salt Lake City, UT, *Elementa: Science of the Anthropocene*, 7, <https://doi.org/10.1525/ELEMENTA.375>, publisher: University of California Press, 2019.
- 500 Lauvaux, T., Miles, N. L., Richardson, S. J., Deng, A., Stauffer, D. R., Davis, K. J., Jacobson, G., Rella, C., Calonder, G.-P., and DeCola, P. L.: Urban Emissions of CO<sub>2</sub> from Davos, Switzerland: The First Real-Time Monitoring System Using an Atmospheric Inversion Technique, *Journal of Applied Meteorology and Climatology*, 52, 2654–2668, <https://doi.org/10.1175/JAMC-D-13-038.1>, publisher: American Meteorological Society Section: *Journal of Applied Meteorology and Climatology*, 2013.
- Lauvaux, T., Miles, N. L., Deng, A., Richardson, S. J., Cambaliza, M. O., Davis, K. J., Gaudet, B., Gurney, K. R., Huang, J., O’Keefe, D., Song, Y., Karion, A., Oda, T., Patarasuk, R., Razlivanov, I., Sarmiento, D., Shepson, P., Sweeney, C., Turnbull, J., and Wu, K.: High-
- 505

- resolution atmospheric inversion of urban CO<sub>2</sub> emissions during the dormant season of the Indianapolis Flux Experiment (INFLUX), *Journal of Geophysical Research: Atmospheres*, 121, 5213–5236, <https://doi.org/10.1002/2015JD024473>, 2016.
- 510 Lian, J., Lauvaux, T., Utard, H., Bréon, F.-M., Broquet, G., Ramonet, M., Laurent, O., Albarus, I., Cucchi, K., and Ciais, P.: Assessing the Effectiveness of an Urban CO<sub>2</sub> Monitoring Network over the Paris Region through the COVID-19 Lockdown Natural Experiment, *Environmental Science & Technology*, p. acs.est.1c04973, <https://doi.org/10.1021/ACS.EST.1C04973>, 2022.
- Mallia, D. V., Mitchell, L. E., Kunik, L., Fasoli, B., Bares, R., Gurney, K. R., Mendoza, D. L., and Lin, J. C.: Constraining Urban CO<sub>2</sub> Emissions Using Mobile Observations from a Light Rail Public Transit Platform, *Environmental Science & Technology*, 54, 15 613–15 621, <https://doi.org/10.1021/acs.est.0c04388>, publisher: American Chemical Society, 2020.
- Mano, Z., Kendler, S., and Fishbain, B.: Information Theory Solution Approach to the Air Pollution Sensor Location–Allocation Problem, *Sensors*, 22, 3808, <https://doi.org/10.3390/s22103808>, number: 10 Publisher: Multidisciplinary Digital Publishing Institute, 2022.
- 515 Miles, N. L., Davis, K. J., Richardson, S. J., Lauvaux, T., Martins, D. K., Deng, A. J., Balashov, N., Gurney, K. R., Liang, J., Roest, G., Wang, J. A., and Turnbull, J. C.: The influence of near-field fluxes on seasonal carbon dioxide enhancements: results from the Indianapolis Flux Experiment (INFLUX), *Carbon Balance and Management*, 16, 4, <https://doi.org/10.1186/s13021-020-00166-z>, 2021.
- Nathan, B. J., Lauvaux, T., Turnbull, J. C., Richardson, S. J., Miles, N. L., and Gurney, K. R.: Source Sector Attribution of CO<sub>2</sub> Emissions Using an Urban CO/CO<sub>2</sub> Bayesian Inversion System, *Journal of Geophysical Research: Atmospheres*, 123, 13,611–13,621, <https://doi.org/10.1029/2018JD029231>, 2018.
- 520 Oda, T., Lauvaux, T., Lu, D., Rao, P., Miles, N. L., Richardson, S. J., and Gurney, K. R.: On the impact of granularity of space-based urban CO<sub>2</sub> emissions in urban atmospheric inversions: A case study for Indianapolis, IN, *Elementa: Science of the Anthropocene*, 5, 28, <https://doi.org/10.1525/elementa.146>, 2017.
- 525 Oettl, D.: Development of the mesoscale model GRAMM-SCI: Evaluation of simulated highly-resolved flow fields in an alpine and pre-alpine region, *Atmosphere*, 12, <https://doi.org/10.3390/atmos12030298>, 2021.
- Richardson, S. J., Miles, N. L., Davis, K. J., Lauvaux, T., Martins, D. K., Turnbull, J. C., McKain, K., Sweeney, C., and Cambaliza, M. O. L.: Tower measurement network of in-situ CO<sub>2</sub>, CH<sub>4</sub>, and CO in support of the Indianapolis FLUX (INFLUX) Experiment, *Elementa: Science of the Anthropocene*, 5, 59, <https://doi.org/10.1525/elementa.140>, 2017.
- 530 Rodgers, C. D.: Inverse methods for atmospheric sounding: Theory and practice, vol. 2 of *Series on Atmospheric, Oceanic and Planetary Physics*, World Scientific Publishing, 2000.
- Super, I., Dellaert, S. N., Visschedijk, A. J., and Van Der Gon, H. A.: Uncertainty analysis of a European high-resolution emission inventory of CO<sub>2</sub> and CO to support inverse modelling and network design, *Atmospheric Chemistry and Physics*, 20, 1795–1816, <https://doi.org/10.5194/acp-20-1795-2020>, 2020.
- 535 Thompson, R. L. and Pisso, I.: A flexible algorithm for network design based on information theory, *Atmospheric Measurement Techniques*, 16, 235–246, <https://doi.org/10.5194/amt-16-235-2023>, 2023.
- Turnbull, J. C., Sweeney, C., Karion, A., Newberger, T., Lehman, S. J., Tans, P. P., Davis, K. J., Lauvaux, T., Miles, N. L., Richardson, S. J., Cambaliza, M. O., Shepson, P. B., Gurney, K., Patarasuk, R., and Razlivanov, I.: Toward quantification and source sector identification of fossil fuel CO<sub>2</sub> emissions from an urban area: Results from the INFLUX experiment, *Journal of Geophysical Research: Atmospheres*, 120, 292–312, <https://doi.org/10.1002/2014JD022555>, 2015.
- 540 Turnbull, J. C., Karion, A., Davis, K. J., Lauvaux, T., Miles, N. L., Richardson, S. J., Sweeney, C., McKain, K., Lehman, S. J., Gurney, K. R., Patarasuk, R., Liang, J., Shepson, P. B., Heimburger, A., Harvey, R., and Whetstone, J.: Synthesis of Urban CO<sub>2</sub> Emission

- Estimates from Multiple Methods from the Indianapolis Flux Project (INFLUX), *Environmental Science & Technology*, 53, 287–295, <https://doi.org/10.1021/acs.est.8b05552>, publisher: American Chemical Society, 2019.
- 545 Turner, A. J., Shusterman, A. A., McDonald, B. C., Teige, V., Harley, R. A., and Cohen, R. C.: Network design for quantifying urban CO<sub>2</sub> emissions: Assessing trade-offs between precision and network density, *Atmospheric Chemistry and Physics*, 16, 13 465–13 475, <https://doi.org/10.5194/acp-16-13465-2016>, 2016.
- Ulrich, V., Brückner, J., Schultz, M., Vardag, S. N., Ludwig, C., Fürle, J., Zia, M., Lautenbach, S., and Zipf, A.: Private Vehicles Greenhouse Gas Emission Estimation at Street Level for Berlin Based on Open Data, *ISPRS International Journal of Geo-Information*, 12, 138, <https://doi.org/10.3390/ijgi12040138>, number: 4 Publisher: Multidisciplinary Digital Publishing Institute, 2023.
- 550 Van Der Gon, H. D., Hendriks, C., Kuenen, J., Segers, A., and Visschedijk, A.: Description of current temporal emission patterns and sensitivity of predicted AQ for temporal emission patterns., 2011.
- Vogel, F. R., Hammer, S., Steinhof, A., Kromer, B., and Levin, I.: Implication of weekly and diurnal <sup>14</sup>C calibration on hourly estimates of CO<sub>2</sub>-based fossil fuel CO<sub>2</sub> at a moderately polluted site in southwestern Germany, *Tellus B: Chemical and Physical Meteorology*, 62, 512, <https://doi.org/10.1111/j.1600-0889.2010.00477.x>, 2010.
- 555 World Bank: Cities and Climate Change: An Urgent Agenda. Urban development series, Urban Development Series Knowledge Papers, <https://openknowledge.worldbank.org/handle/10986/17381>, 2010.
- Wu, K., Lauvaux, T., Davis, K. J., Deng, A., Coto, I. L., Gurney, K. R., and Patarasuk, R.: Joint inverse estimation of fossil fuel and biogenic CO<sub>2</sub> fluxes in an urban environment: An observing system simulation experiment to assess the impact of multiple uncertainties, *Elementa: Science of the Anthropocene*, 6, 17, <https://doi.org/10.1525/elementa.138>, 2018.
- 560 Wu, L., Broquet, G., Ciais, P., Bellassen, V., Vogel, F., Chevallier, F., Xueref-Remy, I., and Wang, Y.: What would dense atmospheric observation networks bring to the quantification of city CO<sub>2</sub> emissions?, *Atmospheric Chemistry and Physics*, 16, 7743–7771, <https://doi.org/10.5194/acp-16-7743-2016>, 2016.
- Öttl, D.: Documentation of the prognostic mesoscale model GRAMM (Graz Mesoscale Model) Vs. 15.12, pp. 1–125, 2020.